MOX-Report No. 23/2015

Anatomy of strong ground motion: near-source records and 3D physics-based numerical simulations of the Mw 6.0 May 29 2012 Po Plain earthquake, Italy

Paolucci, R.; Mazzieri, I.; Smerzini, C.

MOX, Dipartimento di Matematica
Politecnico di Milano, Via Bonardi 9 - 20133 Milano (Italy)

mox-dmat@polimi.it http://mox.polimi.it

Anatomy of strong ground motion: near-source records and 3D physics-based numerical simulations of the M_w 6.0 May 29 2012 Po Plain earthquake, Italy

R. PAOLUCCI[1], I. MAZZIERI[2], C. SMERZINI[3]

May 8, 2015

[1] DICA-Department of Civil and Environmental Engineering, Politecnico di Milano
P.za Leonardo da Vinci 32, 20133 Milan, IT.
roberto.paolucci@polimi.it, chiara.smerzini@polimi.it

[2] MOX–Laboratory for Modeling and Scientific Computing
Department of Mathematics, Politecnico di Milano
P.za Leonardo da Vinci 32, 20133 Milan, IT.
ilario.mazzieri@polimi.it

Keywords: Earthquake ground motion, Site effects, Computational seismology, Wave propagation.

Abstract

Stimulated by the recent advances in computational tools for the simulation of seismic wave propagation problems in realistic geologic environments, this paper presents a 3D physics-based numerical study on the prediction of earthquake ground motion in the Po Plain, with reference to the M_W 6.0 May 29 2012 earthquake. To respond to the validation objectives aimed at reproducing with a reasonable accuracy some of the most peculiar features of the near-source strong motion records and of the damage distribution, this study required a sequence of investigations, starting from the analysis of a nearly unprecedented set of near-source records, to the calibration of an improved kinematic seismic source model, up to the development of a 3D numerical model of the portion of the Po Plain interested by the earthquake, including the irregular buried morphology, with sediment thickness varying from few tens of m to some km. The spatial resolution of the numerical model is suitable to propagate up to about

1.5 Hz. Numerical simulations were performed using the open-source high-performance code SPEED, based on the Discontinuous Galerkin Spectral Elements (DGSE) method. The 3D numerical model coupled with the updated slip distribution along the rupturing fault proved successful to reproduce with reasonable accuracy, measured through quantitative goodness-of-fit criteria, the most relevant features of the observed ground motion both at the near- and far-field scales. These include: (i) the large fault normal velocity peaks at the near-source stations driven by up-dip directivity effects; (ii) the small-scale variability at short distance from the source, resulting in the out-of-phase motion at stations separated by only 3 km distance; (iii) the propagation of prominent trains of surface waves, especially in the Northern direction, induced by the irregular buried morphology in the near-source area; (iv) the map of earthquake-induced ground uplift with maximum values of about 10 cm, in substantial agreement with satellite measurements; and (v) the two-lobed pattern of the peak ground velocity map, well correlated with the distribution of macroseismic intensity.

1 Introduction

Between May and June 2012, a sequence of earthquakes struck a densely populated area in the Po Plain, about 20 km North of Modena and West of Ferrara, in the Emilia-Romagna region, Northern Italy, causing 27 fatalities and substantial damage especially to industrial facilities and historical monuments. The sequence started on May 19 with a local magnitude (M_L) 4.1 earthquake, followed by a M_W 6.1 event (source: Regional Centroid Moment Tensor RCMT, http://www.bo.ingv.it/RCMT) on May 20, at 02:03:53 (UTC), with epicentre near the town of Finale Emilia. The mainshock was followed on the same day by two aftershocks with M_L 5.1, towards East. In the following days, the seismic sequence migrated westward and culminated, on May 29, at 07:00:03 (UTC), with a second relevant shock of M_W 6.0 (source: RCMT), about 10 km SW of the May 20 event, with epicenter close to the municipalities of Mirandola and Medolla. This was followed on the same day by an M_L 5.3 aftershock. On June 3, an M_L 5.1 event, in the municipality of Novi di Modena, closed the Po Plain seismic sequence. The complexity of these events made the macroseismic survey difficult, since the attribution of Mercalli-Cancani-Sieberg (MCS) intensity values was influenced by the cumulative effects of the entire seismic sequence (Galli et al., 2012). For this reason the largest intensity $I_{MCS} = 7 - 8$ was estimated in the municipality of Novi di Modena where the last shock occurred. In spite of relatively modest effects on residential buildings, the earthquakes caused devastating damage to historical and industrial structures, with a dramatic economic impact estimated to about 13 billion Euros of overall loss (Munich RE, 2015).
The seismic sequence occurred in the Southern portion of the Po Plain, a subsident EW trending foreland basin of two opposite verging fold-and-thrust belts, the Southern Alps to the North and the Northern Apennines to the South, which developed in response to the collision of the African and European plates from

the Cretaceous onward (Burrato et al., 2012). The Po Plain is filled by Plio-Quaternary marine and continental deposits, whose thickness ranges from a few tens of m at the top of buried anticlines up to about 8 km in the Eastern part of the basin towards the Adriatic sea (Bigi et al., 1992).
Information on the deep structural geologic setting of the Po Plain has been mostly provided by extensive hydrocarbon exploration (Bigi et al., 1992; Fantoni & Franciosi, 2010) together with the investigations related to the new geological map of Italy (1:50,000 scale, http://sgi.isprambiente.it), while data regarding the superficial stratigraphic sequences come from shallow water wells performed by the Emilia-Romagna region (RER, 1998).
Leaving to other publications (e.g. Boccaletti et al., 2004; Tizzani et al., 2013) a detailed analysis of the seismotectonic and geological framework, we herein summarize its basic features as related to the occurrence of the 2012 Po Plain seismic sequence.
The Northern Apennines frontal thrust system is composed of a pile of NE-verging tectonic units that have developed as a consequence of the Cenozoic collision between the European plate and the Adria plate (Boccaletti et al., 2004). The outermost sector of this system, corresponding to the Po Plain, consists of a complex system of thrust faults and folded arcs, namely, Monferrato, Emilia and Ferrara-Romagna, from West to East, which locally generated structural highs (Figure 1). These buried structures were extensively imaged through seismic reflection lines and deep well logs carried out for hydrocarbon exploration (Pieri & Groppi, 1981). The 2012 Emilia seismic sequence reactivated the basal thrust in the central section of the Ferrara-Romagna arc, as illustrated in Figure 1 around the town of Mirandola. The spatial distribution of the aftershocks together with the available focal solutions indicate that the activated fault system covers a relatively large area elongated in the EW direction (about 50 km long) and consists of nearly EW-striking thrust fault sources dipping South.
The seismic sequence was recorded by different accelerometer networks operating on the Italian territory, making available an unprecedented dataset of recordings in the near field of a thrust event within a region of moderate seismicity and characterized by a very deep sedimentary structure such as the Po Plain. The strong motion (SM) data are numerous, especially for the May 29 earthquake, because many temporary stations were installed in the aftermath of the mainshock of May 20. For this reason, this study is entirely devoted to the analysis of the May 29 earthquake, which is the best documented in terms of SM records and inversion of the seismic source.
From the discussion above, it is clear that the May 29 earthquake presents a series of unique features, that make its study particularly challenging from a scientific point of view, in particular: i) its dramatic impact in a densely populated urban area with a high concentration of industrial activities; ii) the complex geological setting of a deep and large sedimentary basin such as the Po Plain, characterized by a strong variability of sediment thickness from a few tens of meters to about 8 km; iii) the availability of a nearly unique near-fault SM dataset

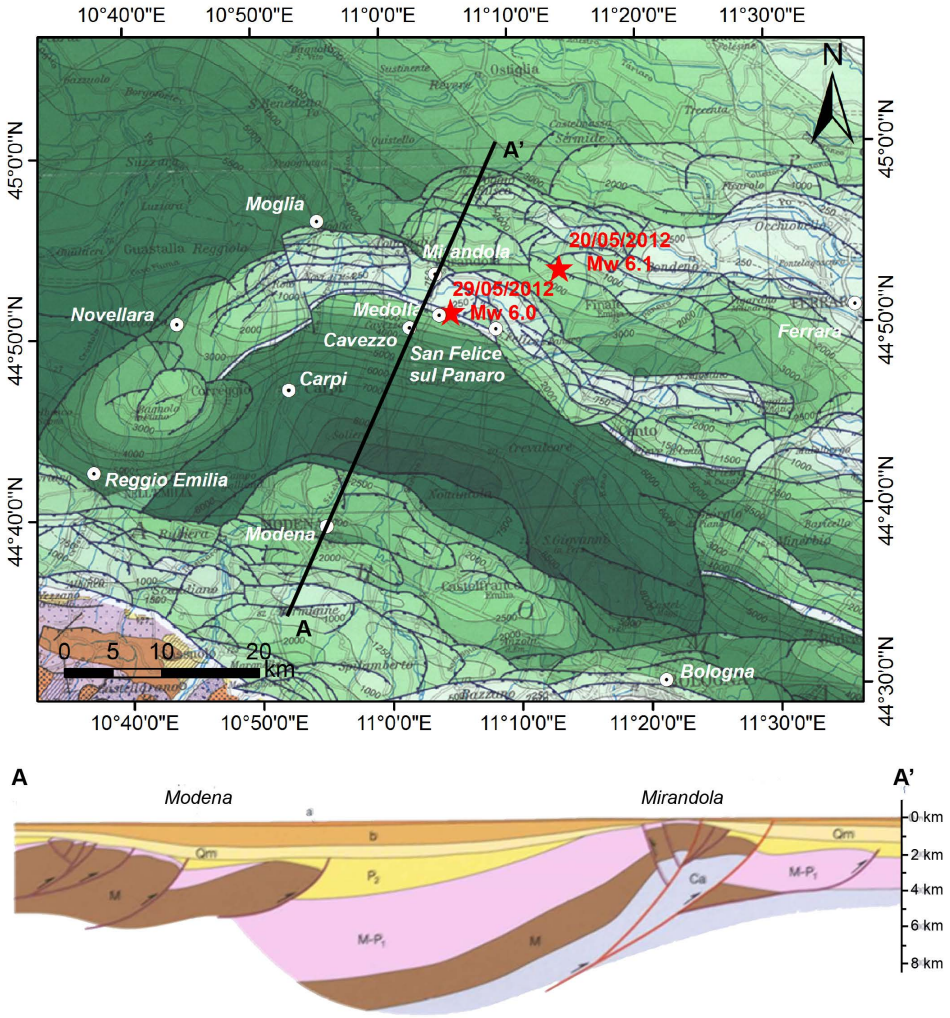

Figure 1: Top panel: structural map of Italy, reproduced from Bigi et al. (1992), where the different shades of green denote the depth of the base of Pliocene; the epicenters (stars) of the two mainshocks of the Po Plain seismic sequence on May 20 (M_W 6.1) and May 29 (M_W 6.0) 2012 are also indicated. Bottom panel: simplified geological cross-section **A-A'** passing through the Ferrara-Romagna folded arc and showing the structural high close to the town of Mirandola (from Boccaletti et al., 2010). a: Middle Pleistocene - Holocene (0.45 My - Present); b: Middle Pleistocene (1 - 0.45 My); Qm: Early Pleistocene (1.8 - 1 My); P2: Middle-Late Pleistocene (4.1 - 1.8 My); M-P1: Late Messinian - Early Pliocene (6.3 - 4.1 My); M: Miocene (24 - 5.4 My); Ca: Meso-Cenozoic Carbonatic Succession (227 - 24 My).

on deep and soft sediments in the context of a region of moderate seismicity.
Stimulated by these considerations, this paper aims at studying within a broad perspective the May 29 2012 Po Plain earthquake, ranging from the analysis of the near-source SM dataset, to the improvement of the available kinematic source models, up to the 3D physics-based numerical simulation of seismic ground shaking. These were performed using SPEED - Spectral Elements in Elastodynamics with Discontinuous Galerkin (http://speed.mox.polimi.it), an innovative high-performance computer code, suitable to tackle multi-scale seismic wave propagation problems in heterogeneous media by a highly accurate numerical integration method based on spectral elements coupled with a DGSE approach. This allows one to include detailed 3D models both of the seismic source and of the source-to-site propagation path. Therefore it is suitable, on one side, to validate the numerical method by comparison with the available records and, on the other side, to shed light on the most salient features of the observed earthquake ground motion in the epicentral area of the May 29 earthquake.
The first section of the paper illustrates the May 29 earthquake SM dataset, focusing on the near-source records and on the spatial distribution of peak ground motion values, in comparison with that provided by Ground Motion Prediction Equations (GMPEs). Then, an updated slip distribution model is introduced, calibrated on the near-source records, which provides evidence of up-dip directivity effects on earthquake ground motion. Finally, 3D physics-based numerical simulations of the May 29 2012 earthquake are presented, spanning a frequency range up to about 1.5 Hz. A thorough check of numerical results vs. records is presented, including comparison in time and frequency domain, as well as quantitative goodness-of-fit tests. Ground motion maps are also presented, in terms of permanent ground uplift and of peak ground velocity, and compared with both instrumental and macroseismic observations.

2 Near-source strong motion records

In this section some features of the near-source strong-motion dataset generated by the May 29 earthquake are addressed. Referring to Luzi et al. (2013) and Castro et al. (2013) for an overview of the SM records of the entire 2012 Po Plain seismic sequence, we have limited our attention to about 30 stations which recorded the earthquake within an epicentral distance $R_e < 30$ km (Table 1). These stations mostly belong to the Italian SM network (RAN) and to temporary networks operated by the Italian Department of Civil Protection (DPC) and by the National Institute of Geophysics and Volcanology (INGV), installed after the May 20 mainshock. Corrected records were downloaded from the Italian Accelerometric Archive ITACA (http:// itaca.mi.ingv.it/).
Stations are classified based on the average shear-wave velocity of the uppermost 30 m, $V_{S,30}$, according to Eurocode 8, EC8 (CEN, 2004). Symbol $*$ in the soil classification means that soil class is inferred from geological considerations,

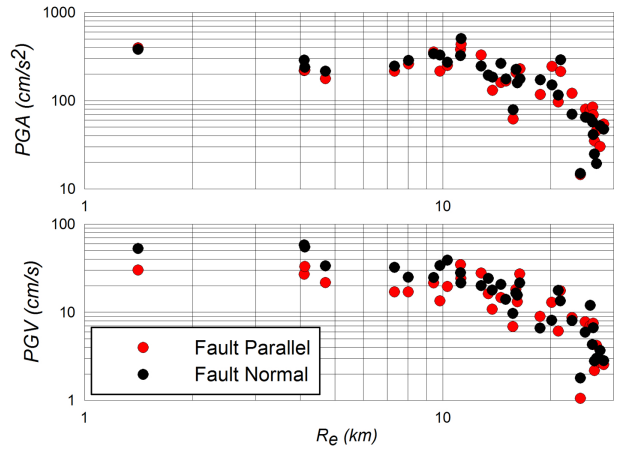

Figure 2: Fault Normal (FN) and Fault Parallel (FP) components of PGA (top) and PGV (bottom) in the selected strong motion dataset of the May 29 2012 earthquake. Data from ITACA database.

rather than being based on direct measurements of the shear-wave velocity. Due to the relatively homogeneous shallow soil conditions throughout the epicentral area, all sites were assumed to belong to soil class C ($180 < V_{S,30} < 360\ m/s$). As a matter of fact, in such area $V_{S,30}$ is typically found to range from 200 to 250 m/s.

For each SM station in Table 1, Peak Ground Acceleration (PGA), Peak Ground Velocity (PGV) and Peak Ground Displacement (PGD) values are provided in terms of the Fault Normal (FN) and Vertical (UP) components, as well as the FN/FP (Fault Parallel) ratio. Note that, since the fault strike is predominantly EW (95°), the FN component is very close to NS. In Figure 2, the variation with R_e of both FN and FP components of PGA and PGV is shown, while, in Figure 3, a representative selection of velocity time histories (NS component) is presented to pinpoint the large variability of amplitude and characteristics of seismic shaking with distance and azimuth. This is also highlighted by the selection in Figure 4, which shows the NS velocity (left) and displacement (right) waveforms recorded by an array of temporary stations (referred to as MIR hereinafter), installed by the INGV rapid response network for site effects EMERSITO, after the May 20 mainshock (Bordoni et al., 2012). The MIR array consists of eight stations aligned along a roughly S-N trending profile, following the direction of increasing thickness of the sediment cover, towards the Po river, from the Mirandola buried structural highs (see Figure 1).

These SM accelerograms form an unprecedented set of near-source records for reverse-fault earthquakes on deep soil configurations, that will be the basis for the validation of the numerical simulations illustrated in the next sections of this study. For sake of brevity, we limit ourselves here to summarize some of their most relevant features:

- prevailing FN motion is apparent in the range $R_e \leq 10\ km$, with FN/FP values increasing when moving from PGA ($\text{FN/FP}_{avg} = 1.2$), to PGV ($\text{FN/FP}_{avg} = 1.8$) and PGD ($\text{FN/FP}_{avg} = 2.0$);

- for $R_e > 10\ km$, FN/FP is significantly larger than 1 ($\text{FN/FP}_{avg} = 1.5$) only for PGD, probably owing to the dominance of long period surface waves propagating northwards, as a consequence of the configuration of the buried topography of the area (see Figure 1);

- velocity pulses with prevailing period of around 1.5 s in the FN direction are evident up to about 5 km distance from the epicenter, while, for increasing distances, trains of surface waves become dominant, as can be clearly seen within the MIR array records (Figure 4);

- very large values of vertical PGA are observed, with an impressive 840 cm/s^2 at MRN, in agreement with the frequent finding, in near-source records, of prevailing vertical PGA with respect to the horizontal one (see e.g. Ambraseys & Douglas, 2003);

- a remarkable small-scale spatial variability is apparent, especially when comparing SM records MIR01 and MIR02 in Figure 4, at some 3 km distance: although records look similar at a first glance, there is a clear out-of-phase motion that suggests a major influence of the focal mechanism itself, with a nodal line probably passing about half way between the two stations.

To investigate in more detail the spatial distribution of earthquake ground motion, with possible combined effect of the seismic source and of the irregular subsoil configuration, recorded peak ground motions are compared to those obtained by the GMPE of Bindi et al. (2014), referred to as BI14 hereafter. The BI14 relationship was derived from Italian data, including the Po Plain seismic sequence. To this end, we computed for each station the ratio of the recorded peak ground motion, i.e., PGA, PGV and $S_a(2s)$, the latter being the pseudo-acceleration response spectral ordinate at $T = 2\ s$, with respect to the corresponding value from the BI14. Predictions are computed for reverse focal mechanisms and for sites C in the EC8 soil classification, considering $M_W = 6$. The Joyner-Boore (R_{JB}) distance, used in BI14, was computed by considering the fault geometry adopted in the numerical model and shown in Figure 3. Note that, although BI14 holds for the geometric mean of the two horizontal components, we decided to compare it with the recorded peak FN values, the geometric mean being hardly meaningful for directional motions in near-source conditions. Figure 5 shows such a comparison, whence it can be deduced that:

- records of the May 29 earthquake have generally lower horizontal PGAs than predicted by BI14, implying possible non-linear effects at high frequencies, although this argument conflicts with the very high accelerations recorded in the vertical direction;

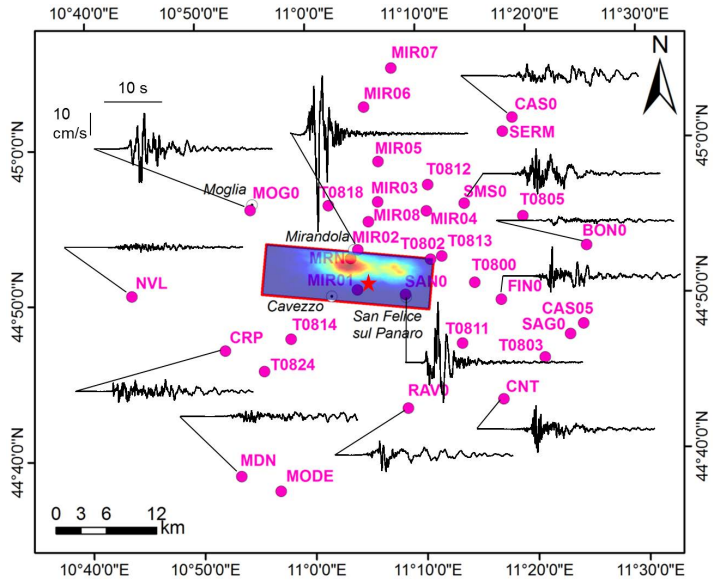

Figure 3: Spatial variability of the NS velocity records in the epicentral area of the May 29 earthquake at selected SM stations. The kinematic fault model, as implemented in the 3D numerical simulations, is also superimposed.

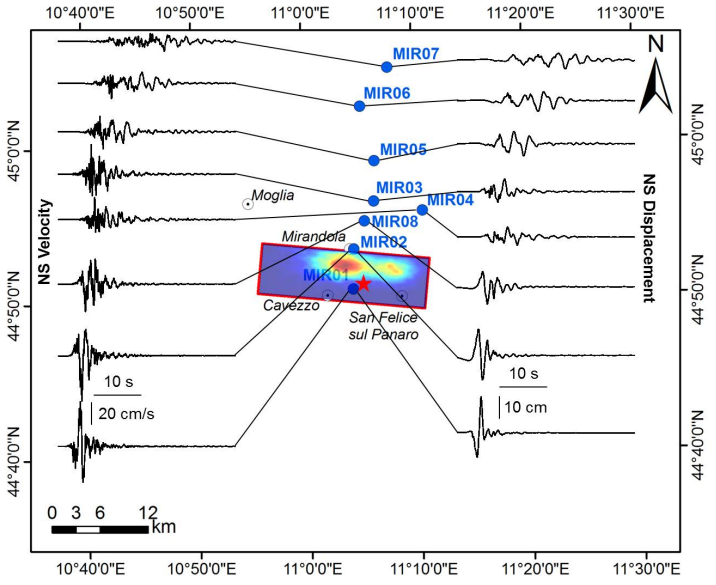

Figure 4: NS records along the MIR transect in terms of both velocity (left-hand side) and displacement (right-hand side) waveforms. The kinematic fault model, as implemented in the 3D numerical simulations, is also superimposed.

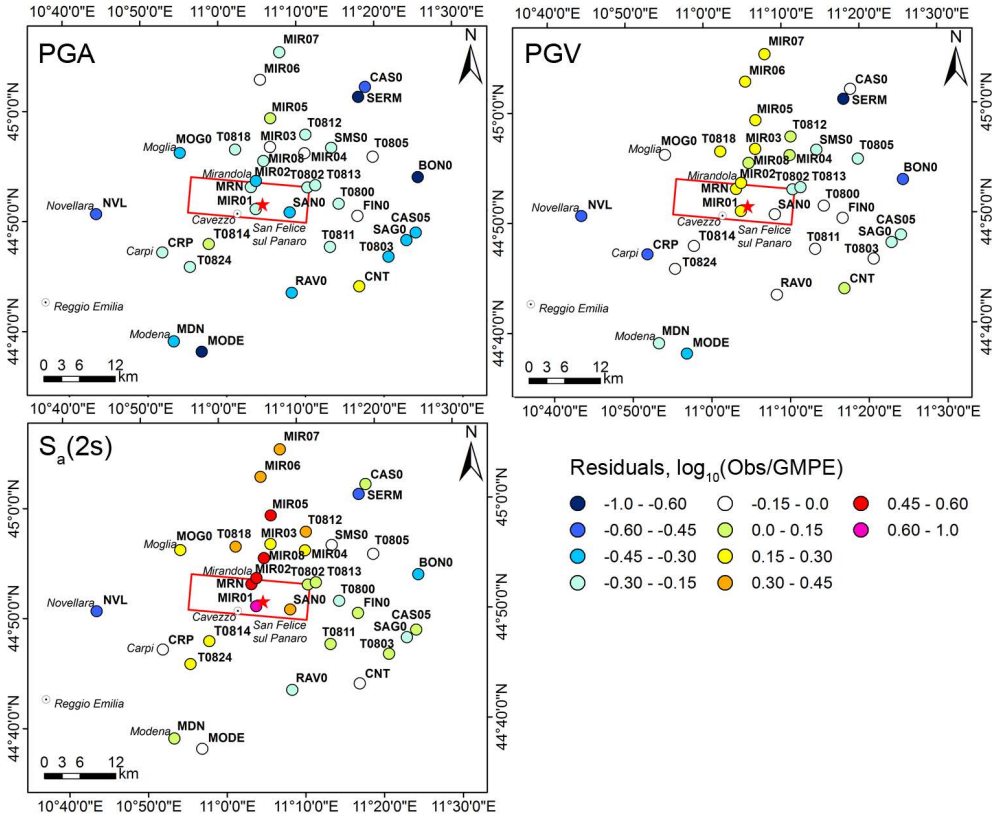

Figure 5: Residuals, computed as log_{10}(observed/predicted), with respect to the GMPE of Bindi et al. (2014). Comparison is made in terms of the observed FN components of PGA (top panel, left), of PGV (top panel, right) and of $S_a(2s)$ (bottom, left).

- PGVs are underestimated by a factor up to about 2, moving Northwards from the seismic source;
- a similar trend as for PGV, although substantially amplified, can be observed also for the $S_a(2s)$ spectral ordinate, for which the underestimation in the stations located North of the seismic source is even larger, reaching up to a factor of 4.

The latter underestimations, either in terms of PGV or $S_a(2s)$, may be mostly attributed to a combination of: (1) the inadequacy of the geometric mean to predict highly directional ground motions in the near-source region, and (2) the inadequacy of $V_{S,30}$ as a proxy for very deep soil sediments, the seismic response of which may be better approximated by assuming soft soil conditions (Class D, $V_{S,30} < 180m/s$).

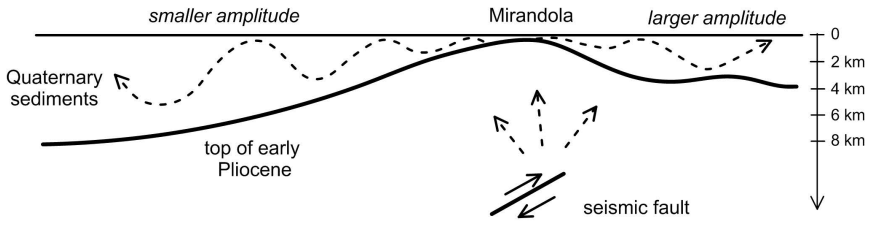

Figure 6: Sketch for interpretation of the observed features of ground motion in terms of coupling of seismic source effects and complex submerged geology.

A sketch summarizing some of the main factors affecting near-source ground motion during the Po Plain earthquake of May 29 is illustrated in Figure 6, with emphasis on the interaction of buried topography with generation of prominent surface waves produced by the highly irregular geological configuration underneath the epicentral region. This sketch clearly points out the need of 3D numerical modelling, to properly simulate the coupling of the kinematics of the seismic source with the complex geologic conditions.
We finally note that one of the clearest features of observed ground motion discussed in this section, i.e., the prevailing FN (roughly NS) component of motion, had a major role on the onset of damage, particularly for those structures responding in the period range from 1 to 2 s where the largest energy content of ground motion was concentrated, as shown by the near-source velocity pulses. This is the case of many churches and industrial pre-cast structures, which actually suffered the highest level of damage during these earthquakes. Figure 7, showing the partial collapse of the San Francesco Church, in Mirandola, only 500 m away from the MIR02 station, provides an impressive example of such damage. As a matter of fact, the nave, with longitudinal axis roughly oriented EW, as in most of the ancient Catholic churches, collapsed in the NS direction, while the facade, much stiffer in its plane, remained nearly intact.

3 Adjustment of the fault-slip parameters based on near-source ground motion records

The adjustment of the slip distribution source model of the May 29 earthquake was by far the most impacting task to obtain an overall satisfactory agreement of the numerical simulations with the near-source records introduced in the previous section.
We started from available models proposed in the literature (e.g., Pezzo et al., 2013), derived from observed coseismic deformations, and checked their accuracy against near-source SM records. To simulate earthquake ground motion we made use of the Hisada approach (Hisada & Bielak, 2003), assuming a horizontally layered crustal model as shown in Table 2. This model approaches,

Table 1: Overview of the SM dataset recorded during the May 29 2012 Po Plain earthquake at epicentral distance $R_e < 30\ km$. Fault Normal (FN), Fault Parallel (FP) and vertical (UP) PGA, PGV and PGD values are provided.

Station Code	Lat ($^\circ N$)	Lon ($^\circ E$)	Soil Class	R_e (km)	PGA_{FN} (cm/s^2)	$\frac{PGA_{FN}}{PGA_{FP}}$	PGA_{UP} (cm/s^2)	PGV_{FN} (cm/s)	$\frac{PGV_{FN}}{PGV_{FP}}$	PGV_{UP} (cm/s)	PGD_{FN} (cm)	$\frac{PGD_{FN}}{PGD_{FP}}$	PGD_{UP} (cm)
MIR01	44.844	11.071	C*	1.41	382.1	0.96	361.5	53.0	1.75	13.8	21.1	2.52	5.1
MRN	44.878	11.062	C	4.10	289.2	1.32	840.6	58.1	2.14	26.8	14.7	1.80	5.8
MIR02	44.887	11.073	C*	4.12	238.8	1.08	452.3	55.2	1.66	12.0	16.3	1.53	5.0
SAN0	44.838	11.143	C*	4.70	217.0	1.22	307.8	33.6	1.55	8.7	10.3	1.22	3.0
MIR08	44.917	11.090	C*	7.33	246.7	1.14	306.7	32.3	1.89	7.8	10.2	3.78	4.2
T0802	44.875	11.182	C*	8.01	286.6	1.10	176.5	25.0	1.46	5.2	7.9	1.29	1.9
T0813	44.878	11.199	C*	9.43	339.6	0.95	171.1	24.8	1.15	3.8	6.2	1.10	2.1
MIR03	44.938	11.105	C*	9.82	328.3	1.52	398.3	34.0	2.52	6.9	7.8	2.28	2.6
T0818	44.935	11.030	C*	10.30	274.3	1.10	210.6	39.1	2.00	6.7	9.0	3.15	3.1
MIR04	44.927	11.178	C*	11.20	324.0	0.85	258.3	28.2	0.81	5.7	6.2	0.83	2.2
T0814	44.793	10.969	C*	11.24	506.1	1.16	252.5	21.6	0.89	6.1	6.3	1.44	1.7
T0800	44.849	11.248	C*	12.80	246.4	0.75	331.8	20.0	0.72	5.0	3.2	0.65	0.8
T0811	44.784	11.227	C*	13.39	195.1	1.00	124.3	24.3	1.49	2.8	4.1	1.38	0.6
T0812	44.955	11.181	C*	13.75	185.6	1.41	108.8	17.8	1.64	2.9	7.1	1.87	1.4
MIR05	44.981	11.107	C*	14.52	264.6	1.64	148.9	20.7	1.41	4.3	7.4	2.30	1.7
SMS0	44.934	11.235	C*	15.00	176.7	1.06	104.3	14.0	1.00	3.0	4.4	1.07	1.1
RAV0	44.716	11.143	C*	15.70	79.0	1.27	61.8	9.7	1.41	1.6	4.3	2.85	1.2
FIN0	44.830	11.287	C*	16.00	226.8	1.09	189.1	16.5	0.91	3.0	2.8	0.90	0.9
T0824	44.759	10.928	C*	16.15	159.2	0.73	96.4	15.6	1.19	2.6	3.0	1.11	0.8
MOG0	44.932	10.912	C*	16.40	176.7	0.77	124.2	21.6	0.79	5.0	6.4	1.92	1.6
CRP	44.782	10.870	C*	18.70	172.9	1.47	83.2	6.6	0.73	2.2	1.9	0.89	0.7
T0805	44.919	11.323	C*	20.15	150.8	0.62	69.2	8.1	0.63	1.5	2.3	0.68	0.7
MIR06	45.040	11.087	C*	21.02	115.7	1.20	89.4	17.8	2.91	2.6	6.3	5.51	1.0
CNT	44.723	11.287	C*	21.30	290.8	1.35	63.8	13.5	0.77	2.6	2.7	0.75	0.7
T0803	44.767	11.351	C*	22.94	70.1	0.58	66.6	8.0	0.92	2.0	2.4	1.49	0.3
SERM	45.010	11.296	C*	24.22	14.9	1.03	9.0	1.8	1.71	0.3	1.0	2.14	0.2
SAG0	44.791	11.390	C*	25.00	64.9	0.81	65.5	5.9	0.76	2.2	1.6	1.02	0.6
MIR07	45.081	11.130	C*	25.80	62.4	0.82	60.9	12.0	1.71	2.7	5.4	2.39	0.7
CAS05	44.802	11.410	C*	26.17	57.4	0.68	46.2	4.3	0.63	1.6	1.4	0.78	0.8
CAS0	45.025	11.311	C*	26.30	41.2	0.60	29.7	6.7	0.88	1.3	3.7	1.75	0.5
BON0	44.886	11.418	C*	26.50	24.8	0.71	30.2	2.8	1.28	1.2	1.5	1.47	0.3
MODE	44.630	10.949	C*	26.87	19.3	0.42	42.3	3.0	0.72	2.2	1.6	0.72	0.8
MDN	44.647	10.890	C	27.50	51.7	1.72	35.1	3.7	1.36	2.0	1.5	1.28	0.6
NVL	44.842	10.731	C	28.10	47.5	0.88	46.2	2.8	1.11	1.1	0.9	1.23	0.3

Figure 7: Collapse of the San Francesco Church (XV century), Mirandola. Courtesy of A. Penna.

Table 2: 1D seismic model adopted for the simulations with the Hisada approach. z_b denotes the depth of the base of the layer

$z_b(m)$	$\rho\ (kg/m^3)$	$V_S\ (m/s)$	$V_P\ (m/s)$	$Q_S\ (-)$
150	1800	250	1500	25
500	2100	800	1800	80
1000	2100	1200	2300	150
3000	2200	2100	3500	200
6000	2400	2750	4750	250
> 6000	2800	3670	6340	350

within the area of Mirandola, the 1D seismic profile estimated by Milana et al. (2014), based on the inversion of SM records and microtremors. For this reason, this model may apply only at few stations, tentatively MIR01, MIR02, MRN and SAN0 (see Figure 3 for location), while, as the thickness of the Quaternary sediments increases, either moving N or S (see Figure 1), a 1D model is no longer suitable to capture the most important features of ground motion, both in terms of frequency and arrival times, as it will be shown later.
By making mostly reference to the previous stations, a trial-and-error procedure was followed to improve the agreement with records by changing the parameters of the main asperities (slip amplitude, depth, along strike position), while keeping the position of the hypocenter unchanged, after verification of consistency of waveform arrivals with the assumed crustal model (A. Herrero, personal communication). The resulting kinematic source model is shown in Figure 8, while the list of source parameters, including fault rupture geometry, location of hypocenter, scalar seismic moment and source time function are shown in Table 3. The source model is characterized by rather shallow asperities, lying at about 6 km depth, which, coupled with the depth of the hypocenter location, may favour up-dip directivity conditions that may explain the large velocity pulses observed

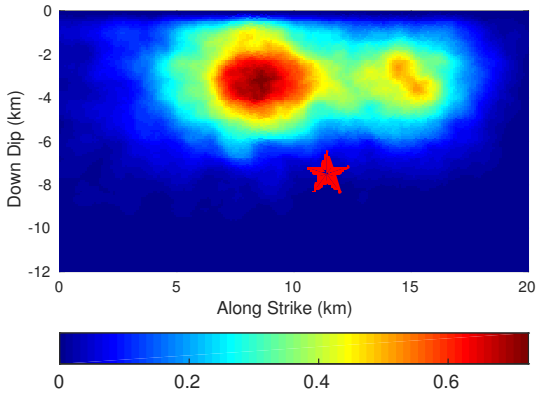

Figure 8: Slip distribution proposed in this work to optimize the agreement with near-source SM records. Scale of slip in m. Note that the vertical axis denotes the down-dip direction, and its origin lies at 3.7 km depth (see Table 3).

in the Mirandola area.

For the final adjustment of the model, the most significant improvement was obtained by studying the sensitivity of the solution with respect to the dip angle. For this purpose, we show in Figure 9 the comparison of NS velocity components at several near-source stations for two different values of the fault dip angle. It can be noted that, in the case of dip = 40°, a good agreement is found for stations MIR01 and SAN0, S of the epicenter. However, moving Northwards, the simulation fails to predict the phases of both MRN and MIR02. A much better agreement is obtained when considering the dip = 60°: in this case, not only the velocity pulse at MRN is captured with a striking detail, but also it is possible to justify the previously noted nearly out-of-phase motion at MIR01 and MRN stations.

Therefore, our results support the interpretation of a steeper fault plane of the May 29 event than initially proposed (e.g., Pezzo et al., 2013). This is in agreement both with Tizzani et al. (2013), who found an optimum fit with InSAR ground deformation measurements from finite element numerical modeling for a dip angle of about 60° (see red line in their Fig. 3h of the quoted paper) and with Govoni et al. (2014), who, based on the accurate aftershock location suggested for the event under study a dip angle equal to 70° (see their Fig. 6).

Note, at top of Figure 9, that 1D finite fault simulation at the MIR08 station, located at about 4 km N of MRN, clearly shows an anticipated trigger of strong motion, while amplitude is reasonably well predicted. This is because the local thickness of the Quaternary sediments (Qm in Figure 9) is much larger than provided by the model of Table 2. By modifying such thickness for the various recording stations and looking for the best fit with records, we were able to constrain with reasonable detail a model for the base of Quaternary sediments, at

Table 3: Fault parameters adopted in the present work.

Fault geometry	Fault parameters	Present Study
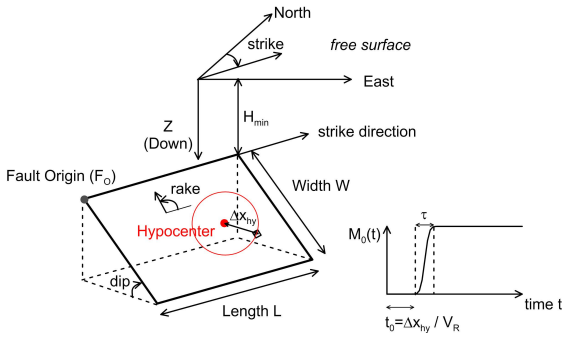	Fault Origin F_O (Lat, Lon)	$(44.895\ N, 10.936\ E)$
	Top Depth of Fault H_{min} (km)	3.7
	Length along Strike L (km)	20
	Width along Dip W (km)	12
	Epicenter (Lat, Lon)	$(44.851\ N, 11.086\ E)$
	Focal Depth (km)	10.4
	Strike $(^\circ)$	95
	Dip $(^\circ)$	60
	Rake $(^\circ)$	90
	Seismic moment M_0 (Nm)	$9.35 \cdot 10^{17}$
	Rise time τ (s)	0.70
	Rupture Velocity V_R (m/s)	$0.85\ V_S$

least in the near-source region, which was subsequently used to define the seismic velocity structure of the 3D numerical model. At MIR08, the best agreement was found for thickness $H = 1\ km$, at MIR02 and SAN0 $H = 0.3\ km$, at MIR01 $H = 0.2\ km$, while the best agreement at MRN was for the model reported in Table 2. As a final remark, we note that, mainly due to the combination of the relatively low values of the seismic velocities with the shallow asperity distribution shown in Figure 8, the rupture velocity turns out to play a key role. Therefore, care was taken to verify the possible onset of super-shear conditions. Such conditions were subsequently ruled out, because they resulted in unrealistically high peaks of motion predicted in the numerical simulations (Figure 10).

4 The Spectral Element Code SPEED

The software package SPEED (http://speed.mox.polimi.it) is apt to simulate seismic wave propagation at local or regional scale. The code is based on a discontinuous version of the classical Spectral Element (SE) method, as explained in Antonietti et al. (2012). SPEED was recently applied to study seismic risk scenarios in large urban areas for reinsurance evaluations (Paolucci et al., 2014), as well as for the analysis of city-site interaction effects related to the dynamic response of large infrastructures (Mazzieri et al., 2013).

The SE method was originally developed in computational fluid dynamics (see Patera, 1984) and then successfully adapted to address seismic wave propagation studies (early applications can be found in Faccioli et al., 1997; Komatitsch & Tromp, 1999; Seriani et al., 1995). Nowadays the SE approach is among the most widely used in computational seismology. For a detailed review, the reader may refer to Komatitsch et al. (2005) and Chaljub et al. (2007) .

The success of the SE method in the scientific community is due to its capability of providing fast and highly accurate solutions (Maday et al., 1989) and its easy

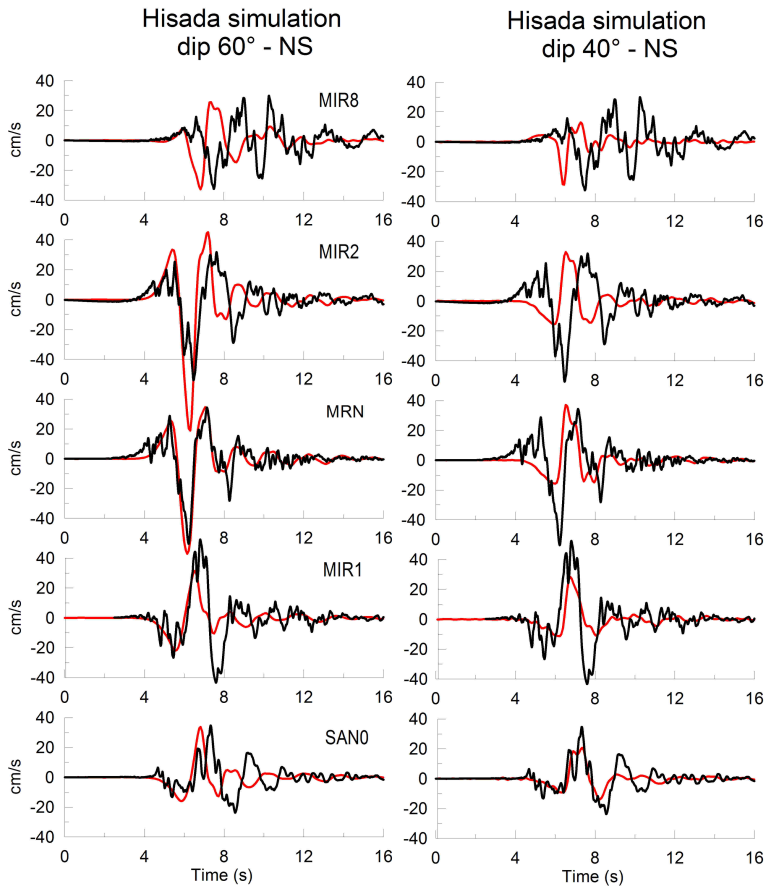

Figure 9: Comparison of NS velocity records (black lines) and numerical (Hisada) results (red lines) obtained using the proposed slip model with fault dip = 60° (left) and dip = 40° (right).

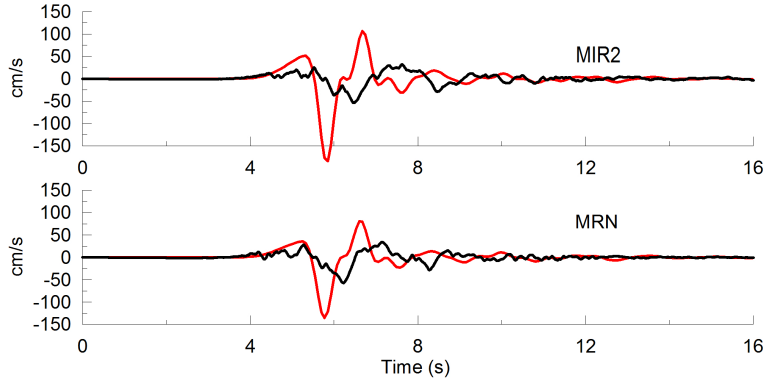

Figure 10: Effect of super-shear rupture velocity, using the fault model proposed in this paper with $V_R = 2800\ m/s$. Super-shear simulations (red lines) largely exceed records (black lines) in the up-dip stations (MIR02 and MRN).

parallel implementation on large supercomputers (Göddeke et al., 2014). To better exploit their intrinsic *hp* nature, SE methods can be extended to address discontinuous approximations (e.g., Käser & Dumbser, 2006; Antonietti et al., 2012; Wilcox et al., 2010; Peyrusse et al., 2014) apt to capture local variations of the physical solutions. The DGSE approaches have been shown to preserve the same accuracy of SE methods and to feature low dissipation and dispersion errors (see, e.g., Antonietti et al., 2012; De Basabe et al., 2008; Hesthaven & Warburton, 2008), so that they guarantee an accurate approximation of amplitudes and phases of the wavefield. On the other hand, DGSE methods are much more flexible than SE methods, since they can handle subdomainwise non-matching grids and different local approximation degrees, making such schemes well suited for simulations with adaptive choice of discretization parameters. More precisely, the spatial discretization and/or the local polynomial degree can be tailored to the region of interest (e.g., buildings or other civil engineering structures in contact with large-scale soil domains). Furthermore, DGSE methods enjoy a high level of intrinsic parallelism, making such a discretization technique well suited for massively parallel computations (Paolucci et al., 2014).
The DGSE method proposed by Mazzieri et al. (2013) has been implemented in SPEED, a certified open-source code for the simulation of seismic wave propagation in three-dimensional complex media as well as soil-structure dynamic interaction problems. SPEED is naturally designed for multi-core computers or large clusters. It is written in Fortran90 using its pseudo-object oriented features. It takes advantage of the hybrid parallel programming based upon the Message Passing Interface (MPI) library, relying on the domain decomposition paradigm and the OpenMP library for multi-threading operations on shared memory. The mesh generation may be accomplished using a third party software, e.g. CUBIT (http://cubit.sandia.gov/) and load balancing is made easier by graph partitioning based on the METIS library (glaros.dtc.umn.edu/) included in the package. The present version of SPEED includes the possibility to treat linear and nonlinear visco-elastic soil materials, either with frequency proportional quality factor (Stupazzini et al., 2009), or frequency constant quality factor (Moczo et al., 2014). Paraxial boundary conditions (Stacey, 1988) reduce spurious reflections from outgoing waves inside the computational domain, while time integration can be performed either by the second order accurate explicit leap-frog scheme or the fourth order accurate explicit Runge-Kutta scheme (see Quarteroni et al., 2007).

5 Setup of the 3D numerical model

The computational domain adopted for the numerical simulation of the M_W 6.0 May 29 earthquake extends over a volume of about $74 \times 51 \times 20$ km^3 and is discretized using an unstructured conforming mesh with characteristic element size ranging from ≈ 150 m at the surface to ≈ 1500 m at the bottom of the

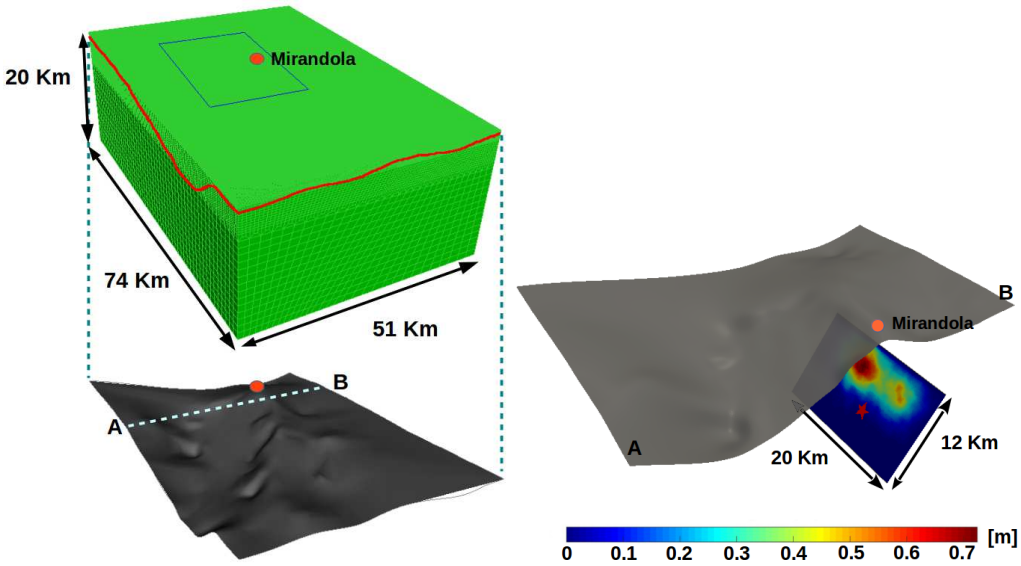

Figure 11: Left, 3D numerical model including the seismic fault responsible of the M_W 6.0 May 29 earthquake and the buried topography, cooresponding to top of the Miocene formations (denoted by M in Figure 1). Right, assumed slip distribution to model the earthquake fault rupture, as described in Section 3 and illustrated in Figure 8.

model, see Figure 11. The mesh was created in order to propagate frequencies up to about 1.5 Hz.

Compared to standard approaches based on plane wave propagation analyses through horizontally layered media, the distinctive features of the numerical model are (see Figure 11): (i) a kinematic representation for the seismic fault rupture of the 29 May earthquake, and (ii) inclusion of a 3D velocity model of the Po Plain, taking into account the spatial variation of the most relevant geologic discontinuities beneath the surface sediments, which have significant effects on the seismic wave propagation. Due to the small topographic variations of the investigated area, a flat free surface has been used, even though SE methods are naturally suited to deal also with surface topography variations.
The adjustment of the kinematic fault model parameters was already introduced and discussed in Section 3, and the resulting model illustrated in Figure 8 and Table 3. Note that, in the 3D simulations, we enhanced the slip distribution by making it compatible with a k^{-2} model, using the approach developed by Herrero & Bernard (1994), in order to improve the high frequency radiation from the seismic source. The source time history is given by an approximate

Heaviside function, as follows:

$$M_0(t) = 1/2 \cdot \left[1 + erf\left(4 \cdot \frac{t - 2\tau}{\tau}\right)\right]$$

where M_0 is the scalar seismic moment, $erf(\cdot)$ is the error function and $\tau = 0.7\ s$ is rise time, assumed to be constant across the fault plane. As previously discussed, to avoid unrealistically high velocity pulses due to super-shear effects (see Figure 10), the rupture velocity was bounded to $V_R = 0.85V_S$, being V_S the shear wave velocity at the corresponding source depth.

To construct the 3D seismic velocity model, two main geologic interfaces were considered. First, the base of Quaternary sediments (z_Q), was estimated from the geological cross-sections available within the study area (see e.g. the bottom panel of Figure 1), combined with the quantitative evaluation of sediment thickness at several selected stations to provide the best fit on near-source records, as mentioned in Section 3. Note that we considered $0.15\ km < z_Q < 2\ km$ throughout the model. Second, the base of Pliocene formations (z_P), was derived from the structural map of Italy (Bigi et al., 1990, 1992, see shaded tones in Figure 1, top panel) and made available as a georeferenced image by P. Burrato (INGV, personal communication). Modelling the variability of the Quaternary sediments thickness throughout a small spatial range around Mirandola, was found to play a key role to simulate with reasonable accuracy the prominent trains of surface waves observed along the MIR array.

Based on the formulas adopted in Table 4, V_S in the Quaternary sediments varies from 300 m/s to 730 m/s, while in the Pliocene layers it varies from 800 m/s to about 1850 m/s, the latter value associated to the maximum depth of the Pliocene, around 7.5 km. A representative NS cross-section of the V_S model, passing through Mirandola, is illustrated in Figure 12. Note that a linear viscoelastic soil model with frequency proportional Q factor has been assumed in these simulations (see Stupazzini et al., 2009).

It should be remarked that the resulting 3D numerical model is a compromise between, on one side, the need to fit as closely as possible the available geological and geophysical information throughout a large spatial region, and, on the other side, to cast such information within a reasonably simple form apt to construct the computational model. For example, note that, to reduce the number of degrees of freedom in the numerical grid, we had to constrain the shear wave velocity in the top layer to a minimum value of 300 m/s.

In spite of such approximations, the numerical model is in reasonable agreement with previously published studies. Namely, we made reference to several 1D profiles available in the Mirandola area (Martelli & Molinari, 2008; DPC-INGV Project S2, 2012; Milana et al., 2014), as well as with the recent work published by Molinari et al. (2015), who calibrated a 3D seismic model for the Po Plain and used it for spectral elements numerical simulations on a much broader area than considered in this paper, albeit with a much lower frequency resolution ($f < 0.33Hz$). A comparison of the V_S profile at Mirandola based on our nu-

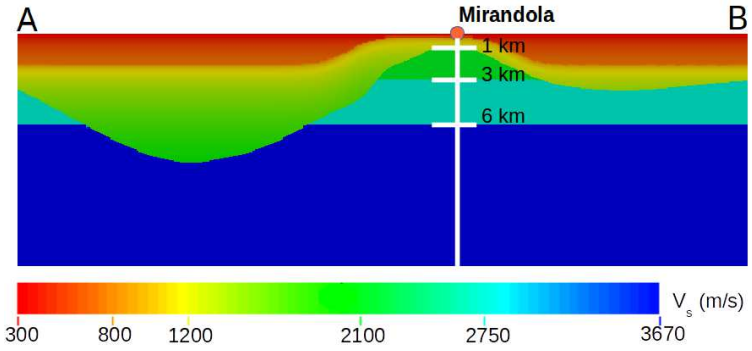

Figure 12: Representative NS cross-section of the numerical model passing through Mirandola, showing the V_S model adopted in the 3D numerical simulations for both Quaternary-Pliocene deposits and bedrock older formations.

Table 4: Dynamic properties of the geologic formations in the 3D numerical model. z_Q and z_P denote the base of Quaternary (Q_M in Figure 1) and Pliocene (M-P_1 in Figure 1) soil units

Geologic Unit	Depth z (m)	ρ (kg/m^3)	V_S (m/s)	V_P (m/s)	Q_S $(-)$
Quaternary	$z < 150$	1800	300	1500	30
	$150 < z < z_Q$	$1800 + 6\sqrt{z - 150}$	$300 + 10\sqrt{z - 150}$	$1500 + 10\sqrt{z - 150}$	$V_S(z)/10$
Pliocene	$z_Q < z < z_P$	$2100 + 4\sqrt{z - z_Q}$	$800 + 15\sqrt{z - z_Q}$	$2000 + 15\sqrt{z - z_Q}$	$V_S(z)/10$
before Pliocene	$z > z_P$	see seismic model in Table 2 at corresponding depth			

merical model and the inversion published by Milana et al. (2014) is shown in Figure 13. There is an overall good agreement, except for the $1 - 2$ km depth range, where our values are significantly larger than those of Milana et al. (2014). However, we verified that such disagreement has only a minor influence on the numerical results.

Finally, the seismic velocity model was implemented into a numerical spectral element model. Considering a rule of thumb of 4 grid points per minium wavelength for non dispersive wave propagation in heterogeneous media by the SE approach (Faccioli et al., 1997), and considering a maximum frequency $f_{max} = 1.5$ Hz, the model consists of $1'975'240$ spectral elements, resulting in approximately $150 \cdot 10^6$ degrees of freedom, using a third order polynomial approximation degree. The time integration has been carried out with the leap-frog scheme, choosing a time step equal to 0.001 s for a total observation time $T = 30$ s. The simulations have been carried both on the Idra cluster located at MOX-Laboratory for Modeling and Scientific Computing, Department of Mathematics, Politecnico di Milano (http://hpc.mox.polimi.it/hardware/) and on the Fermi cluster located at CINECA, Bologna, Italy (http://www.hpc.cineca.it/). As indicator of the parallel performance of the code SPEED, we report in Table 5 the total simulation time (walltime) for a single run of the Emila earthquake,

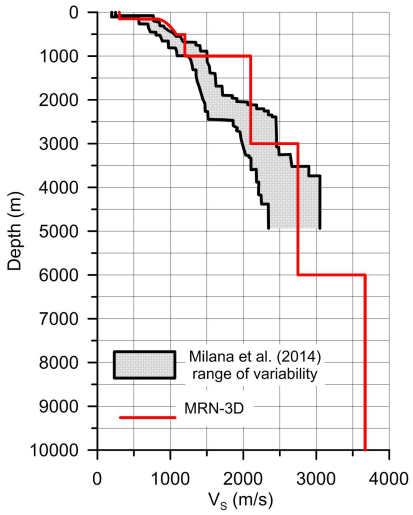

Figure 13: Comparison between the V_S profile implemented in the 3D numerical simulations and the 1D average best model proposed by Milana et al. (2014) for the Mirandola area.

Table 5: Walltime for a single simulation of the Emilia earthquake, performed both on Fermi (CINECA) and Idra (MOX) clusters.

Cluster	Cores	Walltime (hours)
Fermi (CINECA)	4096	4.98
Idra (MOX)	72	19.83

considering both Fermi and Idra clusters.

6 Numerical results and comparison with records

Physics-based numerical simulations have the power to provide a complete picture of ground motion, including its spatial variability on a wide scale, that cannot be achieved by any other approach for earthquake ground motion prediction. As an example, in Figure 14 several snapshots are shown representing the horizontal (FN) velocity wavefield on a NS cross-section passing through the Mirandola anticline and through some of the most representative strong motion stations considered in this work (MIR01, MIR02 and MIR08, as indicated on the map). The snapshots point out the predominant role played by the up-dip source directivity coupled with the irregularity of the buried bedrock configuration, leading, on one side, to the largest velocity peaks at the up-dip stations, and, on the other side, to the generation of trains of surface waves propagating from both N and S sides of the Mirandola high, but with largest peaks in the N direction, as a consequence of the up-dip directivity. The zoom of the velocity

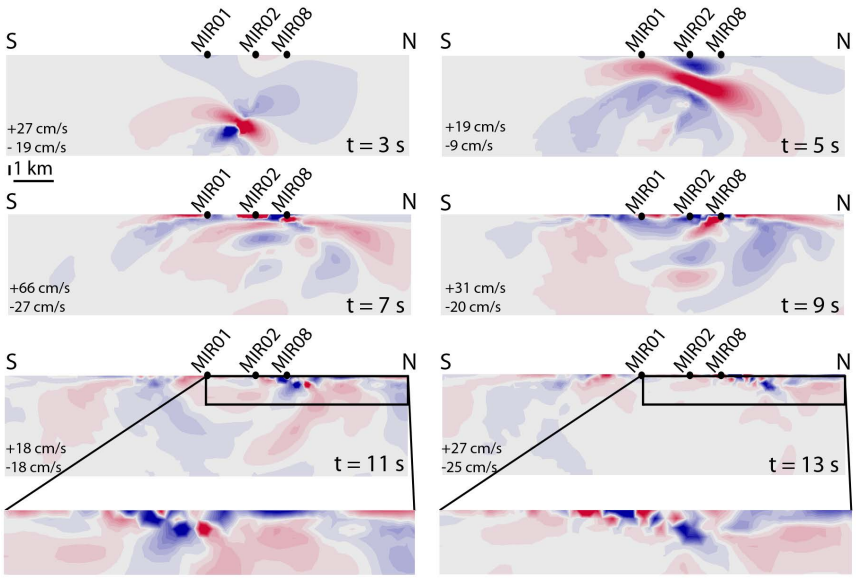

Figure 14: Snapshots of the horizontal (FN) velocity wavefield across a NS cross-section passing through the Mirandola high. Note the different scales of the plots.

field within the top Northern portion of the cross-section (bottom side of Figure 14) allows one to point out also the dispersive features of surface wave propagation, with long period/wavelength components travelling faster away from the source than the short period ones. After having highlighted through the previous figure some general features of the seismic wave propagation problem, we aim now at illustrating in more detail the results of the numerical simulations and at comparing them with SM records. Specifically, we show in Figure 15 the three-component velocity waveforms and in Figure 16 the corresponding Fourier Amplitude Spectra (FAS) at ten representative SM stations. The latter were chosen to provide a relatively uniform sample in terms of their geographic distribution. Both recorded and simulated waveforms were band-passed filtered with an acausal Butterworth 3^{rd} order filter between 0.1 and 1.5 Hz, the latter being the frequency resolution of the numerical model.
On the whole, the agreement between synthetics and records is good, especially on the horizontal NS and vertical component for almost all considered stations. In particular, the agreement of the NS velocity pulse, with PGV around 55 cm/s at the closest stations to the epicentre (i.e., MRN and MIR01) is remarkable and proves the effect of up-dip directivity from the slip distribution model established in Section 3. While leaving to the following section some comments on the prediction of the vertical components of motion, which is also very satisfactory, we note that we did not succeed to obtain a similar good agreement on the EW component, especially at those stations located at short epicentral

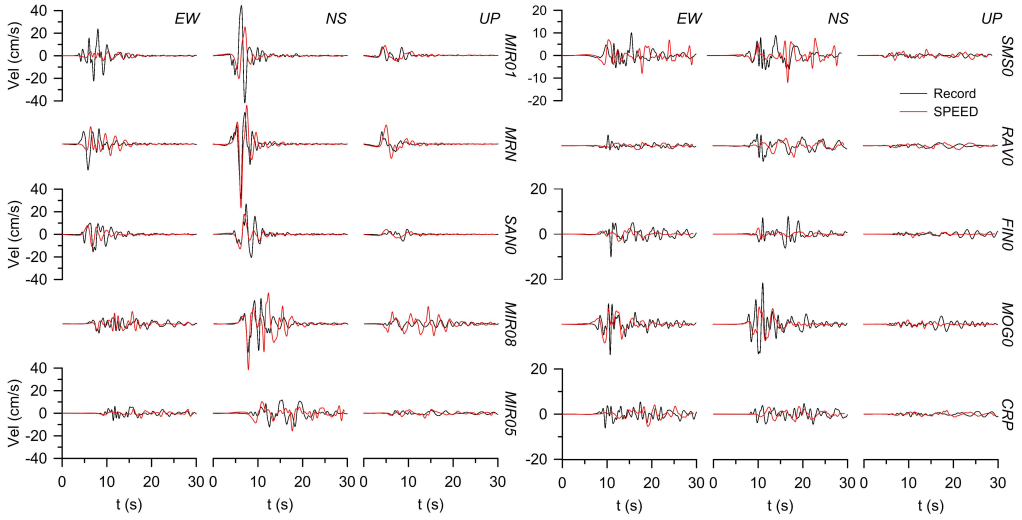

Figure 15: Comparison between recorded (black line) and simulated (red line) three-component velocity waveforms for a representative subset of ten SM stations.

distance ($R_e < 5\ km$), such as MRN and MIR01, while the comparison improves at other stations. Given the short distance to the source, such discrepancies are likely related to details of the slip distribution and/or of the complex buried morphology, which may not be properly accounted for in the numerical model. The analysis of ground motion along the MIR transect is particularly meaningful and it is shown in Figure 17, where the recorded and simulated three-component displacement time histories in the frequency range $0.1 - 1.5\ Hz$ along such transect are compared, with the exception of station MIR07, which falls out of the numerical model. It is found that numerical simulations provide a reasonably good prediction of one of the most significant features shown by the May 29 SM dataset, i.e., the onset of a train of Northwards propagating surface waves, generated by the buried morphological irregularity of the Mirandola structural high (see sketch in Figure 6). In the epicentral region, body and surface waves overlap, while the latter become predominant at distances larger than about 10 km, as highlighted by the long period components in the coda of the signals. As remarked previously, EW components at these close-by stations are poorly predicted. Similar conclusions on the role of the buried morphology on the onset of surface waves during the Po Plain earthquakes were recently pointed out by Molinari et al. (2015), the numerical results of which however were limited to the period range $T > 5\ s$ and far away from the seismic source. The overall performance of the numerical simulations was evaluated in a quantitative way using the Goodness of Fit (GoF) criteria proposed by Anderson (2004). For the frequency band of interest (i.e., $0.1 - 1.5\ Hz$), a GoF score from 0 to 10 (< 4,

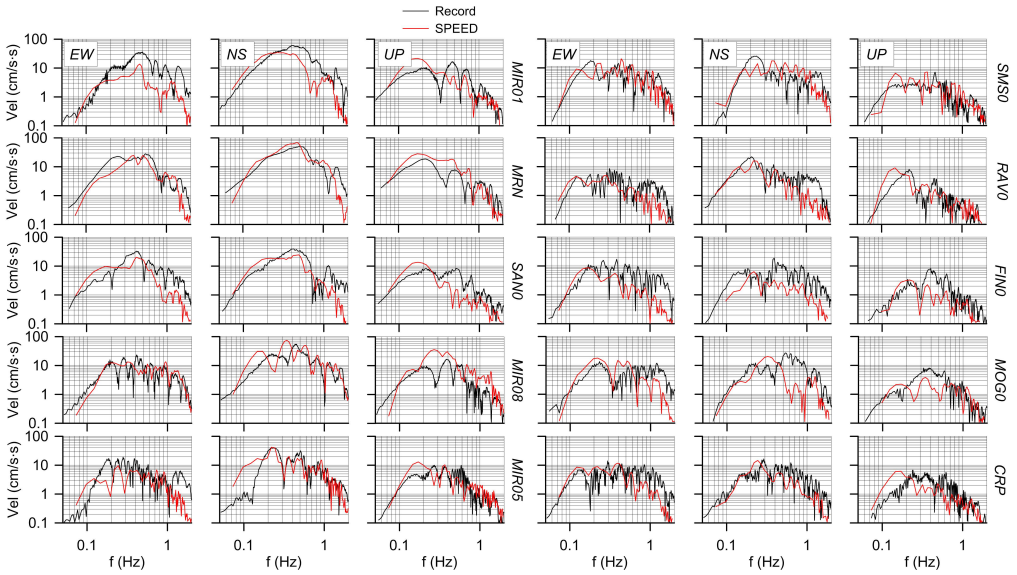

Figure 16: As in Figure 15 but in terms of Fourier Amplitude Spectra (FAS) of velocity signals.

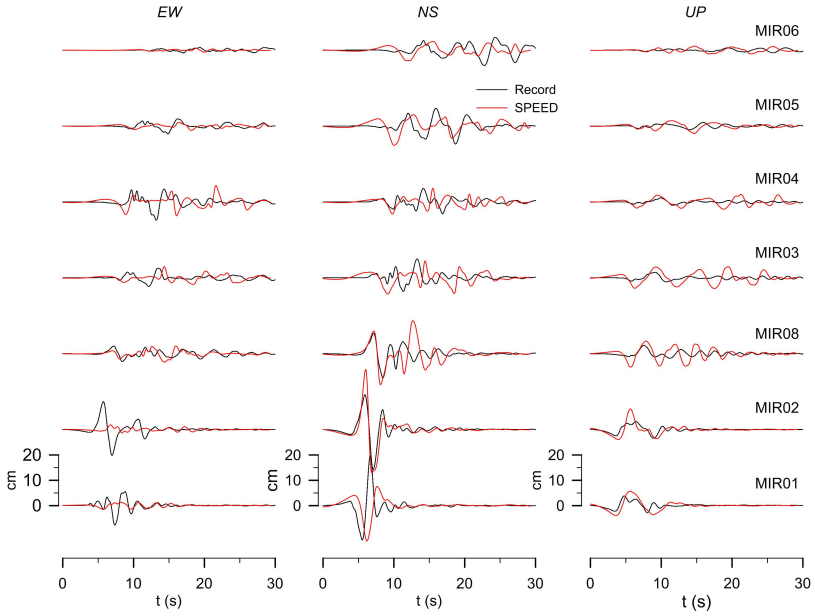

Figure 17: Comparison between recorded (black line) and simulated (red line) three-component displacement waveforms along the MIR transect.

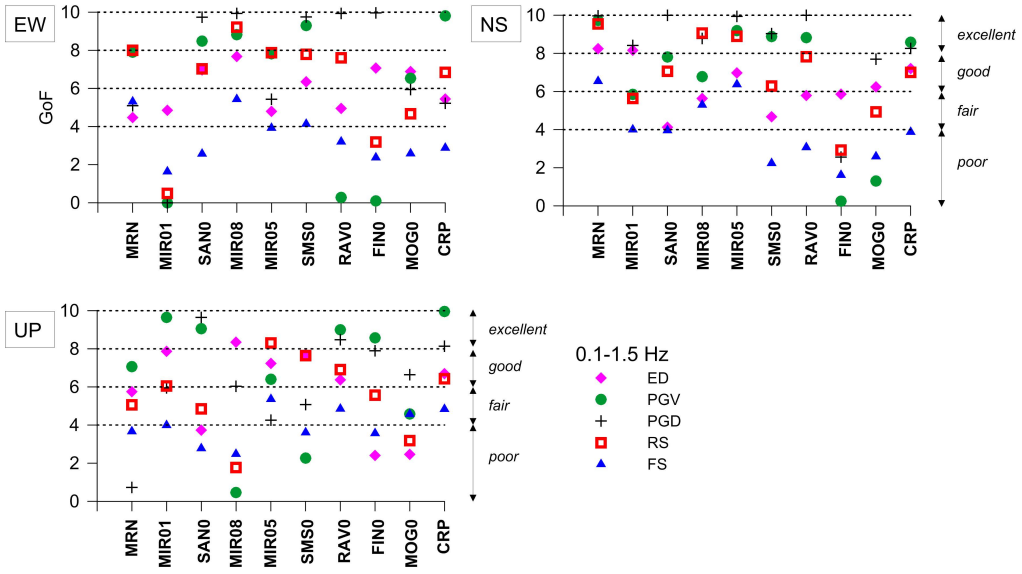

Figure 18: Goodness of Fit (GoF) scores evaluated according to Anderson (2004) at ten SM stations for five criteria, Energy Duration (ED), Peak Ground Velocity (PGV), Peak Ground Displacement (PGD), Response Spectra (RS) and Fourier Spectra (FS), and for the three components of motions (horizontal EW and NS, top panel; vertical, bottom panel).

poor; $4-6$, fair; $6-8$, good; ≥ 8, excellent) is estimated on five metrics of interest for engineering purposes, namely: energy duration (ED), peak ground velocity (PGV), peak ground displacement (PGD), response spectral acceleration (RS), and Fourier Amplitude Spectrum (FAS). Note that FAS and RS criteria are evaluated considering only the frequencies and structural periods within the range $0.1-1.5\ Hz$ of validity of the numerical simulations. The GoF scores, computed for each criteria and for the three components of motion, are shown in Figure 18 for the same subset of ten SM stations as considered in Figures 15 and 16. These results confirm that:

- with few exceptions, the numerical model provides predictions that are in overall good agreement (from fair to excellent) with the SM records;
- results for the NS component are significant better than those for other components. With the exception of stations FIN0 and MOG0, the average GoF scores are in the range from good to excellent;
- results for the EW and vertical components have an average GoF score from fair to good and show a larger scatter among the considered criteria.

To have a broader view of the misfit between records and simulated results at territorial scale, we present in Figure 19 the maps of the GoF scores computed

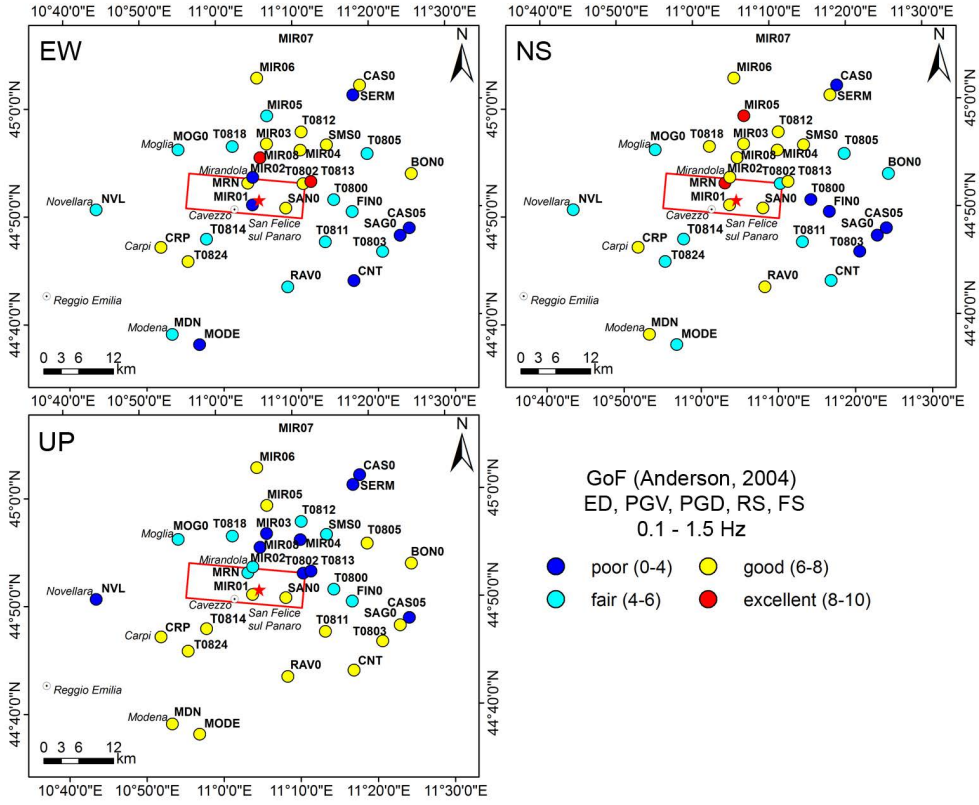

Figure 19: Map of GoF scores for all available SM stations at $R_e < 30\ km$ for EW, NS and vertical components.

as average of the five metrics under consideration for the EW, NS (top panel) and vertical (bottom panel) components at all available SM stations at $R_e < 30\ km$. It is found that for the majority of stations the agreement between simulations and observations is from fair to good, with best results on the NS component, as already noted previously. A poor agreement is found at some sites but it is relevant to underline that average scores below 4 are never determined simultaneously on all components (apart from station CAS05 showing unusual large amplitude waves in the coda of the signal).

7 Prediction of earthquake-induced ground uplift

As a key benchmark to assess the accuracy of the proposed fault model and the performance of the numerical simulations at very low frequencies, we address in this section the comparison of the numerical results with the ground deformation maps produced starting from the aftermath of the May 20 mainshock

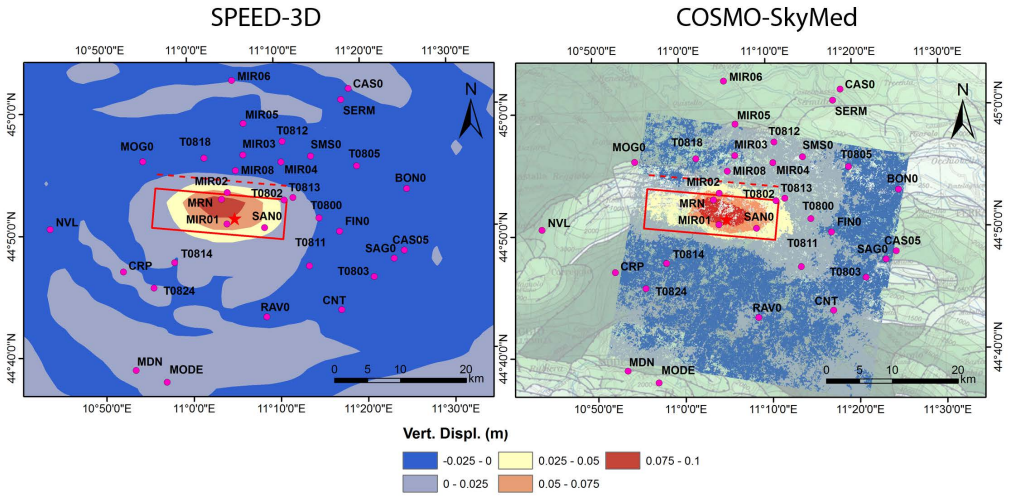

Figure 20: Map of permanent ground uplift simulated by SPEED (left) and observed by COSMO-Skymed InSAR processing (right). In both maps the surface projection of the fault area is shown, together with the intersection of the fault plane with ground surface (dashed line).

(Salvi et al., 2012; Pezzo et al., 2013), taking advantage of the Synthetic Aperture Radar (SAR) Interferometry survey activated by the Italian Space Agency, with the coverage of all four Constellation of Small Satellites for the Mediterranean Basin Observation satellites (COSMO-SkyMed). In Figure 20 (right hand side) the corrected Cosmo-Skymed map is shown, providing detailed measures of ground uplift during the May 29 earthquake, with maximum values slightly exceeding 10 *cm* within the epicentral area. On the left hand side of the same figure, the numerical simulations results are also shown. These are computed by the values of the simulated vertical displacements, averaged over the last 5 seconds of the simulation, after ground shaking has ended. A remarkable agreement is found, except for a slight under-evaluation of uplift in the Western side of the fault area.

As a further verification of the fit of the numerical simulations to the observations, the simulated vertical displacement time histories were compared with displacement records obtained by double integration of accelerations. To avoid losing the information of permanent displacement by high-pass filtering, uncorrected acceleration records were simply processed through a piecewise baseline correction, applied on the velocity trace. Further details on such processing can be found in Maini (2015). Results, illustrated in Figure 21, confirm, on one side, that the baseline processing was successful in reproducing permanent ground deformations close to those inferred from InSAR processing, and, on the other side, the good performance of the numerical model.

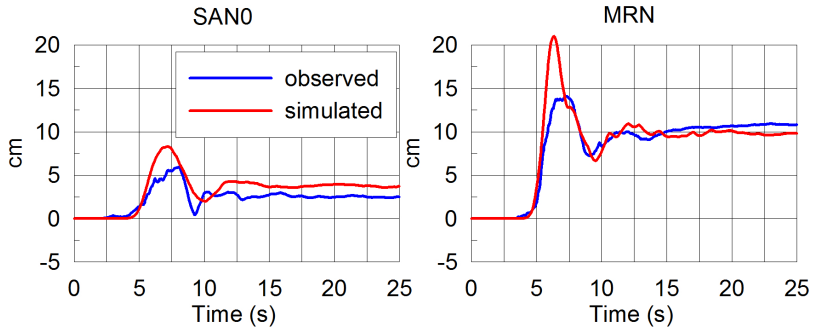

Figure 21: Comparison of observed (blue line) and simulated (red line) vertical displacement time histories at two near-source recording stations (left, SAN0; right, MRN). Acceleration records were processed by a piecewise baseline correction, suitable to recover permanent displacements.

8 Ground shaking and I_{MCS} maps

As a final comparison between simulations and observations, Figure 22 (left panel) illustrates the spatial distribution of PGV (gmh = geometric mean of horizontal components), as predicted by our physics-based 3D numerical simulations. For comparison, the observed gmh values of PGV, obtained at the available SM stations in the same frequency range of 3D numerical simulations, are depicted by filled dots. The simulated ground shaking map shows a characteristic two-lobed pattern (as highlighted within the superimposed box), with maximum amplitudes concentrated within two regions, W and E of the mainshock epicenter. Maximum gmh PGV values of about 60 cm/s are found, in agreement with ground motion recordings. The comparison with the available SM data points out that the overall spatial distribution of simulated ground motion matches reasonably well the recorded one both at the near- and far-field scales. Note that, to produce the map in Figure 21, both numerical results and records have been low-pass filtered at 1.5 Hz, for consistency with the spatial resolution of the numerical mesh. However, the effect of such filter on PGV is limited, while it was not possible to produce a similar map in terms of PGA.
It is worth noting that the two-lobed pattern of gmh PGV turns out to be fairly consistent with the spatial distribution of macroseismic intensity, I_{MCS}, depicted in Figure 22, on the right panel. The map was generated by spatial interpolation of the I_{MCS} data, as provided by the DPC macroseismic survey (Galli et al., 2012), using the spline method implemented in ArcGIS (http://www.arcgis.com). This shows the largest concentration of damage in two NS-elongated areas, one passing through Cavezzo and Mirandola, West of the epicenter, and the second passing through San Felice sul Panaro, East of the epicenter. Note that the I_{MCS} map shows the combined effects of the entire seismic sequence from May 20 to June 3, 2012. This is the reason why, rather

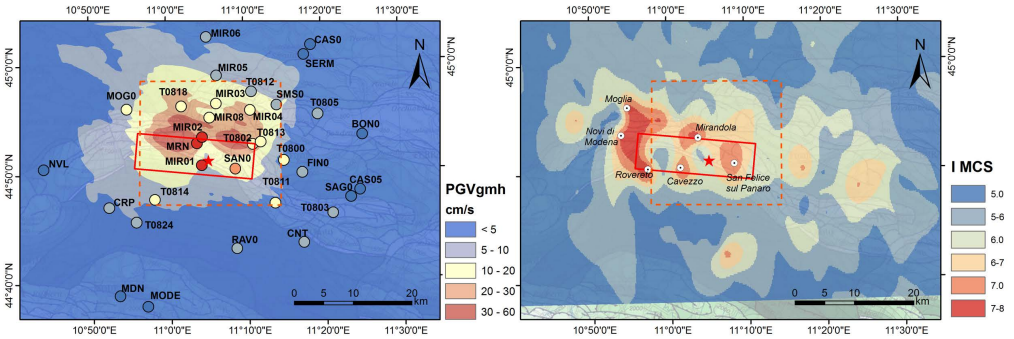

Figure 22: Left, spatial distribution of PGV (gmh = geometric mean of horizontal components) from physics-based 3D numerical simulations. The observed values of gmh PGV (see filled dots), obtained at the available SM stations, are also superimposed for comparison purposes. Right, I_{MCS} map for the whole May-June 2012 seismic sequence. The superimposed box on both panels denotes the region that is mostly associated to the 29 May earthquake.

surprisingly, the heaviest damage occurred in the small area West of Mirandola, in the municipality of Novi di Modena. As a matter of fact, the last shock of June 3, M_L 5.1, acted on buildings slightly damaged by the previous shocks, but which could not withstand the very last one. Therefore, although the cumulative effects of the sequence prevent an accurate discrimination of the impact of the May 29 earthquake alone, the area mostly affected by this earthquake can be roughly included within the dashed quadrangular box in Figure 22. The similarity of the two-lobed patterns of both the PGV and of the I_{MCS} map is worth to be noted, and it may confirm that the pronounced spatial variability of the distribution of damage is likely to be strongly related to the focal mechanism of the earthquake, rather than to amplification effects associated to local site conditions, which are fairly homogeneous throughout the epicentral area.

9 Concluding remarks

3D physics-based numerical simulations of earthquake ground motions are deemed to become in the next future the tool to produce realistic, albeit artificial, scenarios of future earthquakes. This is expected to have a deep impact in terms of creation of earthquake scenarios for seismic risk analyses in large urban areas or for critical structures and infrastructures. Also, this is expected to provide the key to improved predictions of ground motion, and better constrained hazard assessment (Villani et al., 2014), in those conditions that are poorly covered by available worldwide records, such as near-source locations coupled with complex shallow geology.
Several research groups worldwide have developed numerical codes to carry out

such simulations, which typically require high-performance computing tools, and the number of applications for earthquake ground motion predictions in different parts of the world is ever growing (see e.g. Paolucci et al., 2014, for a review). However, for the use of such tools to be accepted in the engineering world, the frequency range of the analyses must be as large as possible to encompass the seismic response of different types of structures. This requires the seismic source to be complex enough to radiate a sufficiently wide frequency spectrum as well as the geological model to be sufficiently detailed to capture reasonably well the complexity of real configurations. And, last but not least, such numerical tools need to be validated against near-source records from real earthquakes, i.e., in those conditions that are mostly relevant for the engineering applications, for their capabilities and limitations to be thoroughly understood and, possibly, overcome.

The M_W 6.0 May 29 2012 Po Plain earthquake, treated in this work, appeared to be one of the most challenging case studies for this purpose, not only because of the availability of a nearly unprecedented number of near-source records, but also because the subsoil conditions of the Po Plain are well known, so that construction of a 3D numerical model including its complex buried morphology was possible with a relatively small effort.

In spite of the availability of the 3D subsoil model and although preliminary fault slip distribution models were made available soon after the earthquake, the numerical modelling task was heavy and the results presented in this work are the fruit of a complex and demanding work, where the most relevant details of strong motion records were carefully and systematically compared with the numerical results, to possibly capture the reasons of the observed discrepancies and to adjust the numerical model consequently.

Eventually, some important evidence of the observed earthquake ground motion was accurately reproduced, such as the large FN velocity peaks at the up-dip stations, the striking out-of-phase motion at the close-by stations MIR01 and MIR02, the pronounced buried topography-induced surface wave trains propagating Northwards and dominating ground motion already at some 10 km distance from the epicenter, the map of ground uplift on the hanging wall side of the fault, the two-lobed pattern of I_{MCS} intensities, well correlated with the gmh PGV map from numerical simulations.

Such good results were obtained by introducing some significant updates of the slip distribution model (Figure 8), adjusted by a trial-and error procedure until a satisfactory result was obtained on the observed near-source velocity waveforms, and by tuning the rapidly varying thickness of Quaternary sediments in the epicentral area, which increases within few km from around 150 m to some 2 km, affecting significantly the accuracy of results.

Probably, the most deceiving results were obtained in terms of the EW components of records closest to the epicenter, especially along the MIR transect, oriented NS and nearly passing through the epicenter. We interpret such disagreement in terms of the insufficient complexity both of the seismic fault and of

the geological model, the latter one consisting of a pretty regular ridge elongated roughly EW. In such conditions, because of a nearly symmetric configuration of both the slip distribution and of the 3D numerical model in the epicentral area, the simulated EW components at the MIR transect turn out to be negligible, contrary to the observational evidence.
A sensitivity study with respect to several numerical modelling assumptions was also made, with respect to the "basic" assumptions of linear visco-elastic materials presented in this work. Namely, a paper in preparation will focus on the effect of: (1) different assumptions of the frequency dependence of the quality factor, Q; (2) the non-linear modelling of the seismic response of shallow soft soil sediments; (3) the spatially correlated random source parameters, for the high frequency content of the seismic radiation to be enhanced; (4) the influence of the seismic velocity model.

10 Acknowledgements

This research has been partly funded by ENEL, Italy, under contract n. 1400054350, in the framework of the international SIGMA Project, and by the Italian Department of Civil Protection, in the framework of the DPC-RELUIS (2014) RS2 Project. Authors are indebted to different researchers of INGV, namely André Herrero, for providing the program to create the k^{-2}slip distribution and for verifying the compatibility of the hypocenter location with the numerical model, Francesca Pacor for different suggestions throughout the work, Simone Atzori for providing the initial slip distribution model, Giuseppe Pezzo, for the COSMOS-Skymed data, and Piefrancesco Burrato, for the georeferenced map of the structural model of the Po plain. The authors extend their gratitude to Ezio Faccioli, for fruitful comments and for the careful review of the manuscript. Strong motion records were downloaded from the ITACA database (http://itaca.mi.ingv.it). Finally, the CINECA award under the LISA and ISCRA initiatives is also gratefully acknowledged, for the availability of high performance computing resources and support.

References

Ambraseys, N. & Douglas, J., 2003. Near-field horizontal and vertical earthquake ground motions, *Soil Dynamics and Earthquake Engineering*, **23**, 1–18.

Anderson, J. G., 2004. Quantitative measure of the goodness-of-fit of synthetic seismograms, in *Proceedings of the 13th World Conf. on Earthquake Engineering*, 16 August 2004, Vancouver, British Columbia, Canada, Paper No. 243.

Antonietti, P. F., Mazzieri, I., Quarteroni, A., & Rapetti, F., 2012. Non-

conforming high order approximations of the elastodynamics equation, *Comput. Meth. Appl. Mech. Eng.*, **209-212**(0), 212 – 238.

Bigi, G., Cosentino, D., Parotto, M., Sartori, R., & Scandone, P., 1990. Structural model of Italy and gravity map, 1:500,000, *Quaderni di Ricerca Scientifica*, **114**(3).

Bigi, G., Bonardi, G., Catalano, R., Cosentino, D., Lentini, F., Parotto, M., Sartori, R., Scandone, P., & Turco, E. E., 1992. *Structural model of Italy 1:500,000*, CNR Progetto Finalizzato Geodinamica.

Bindi, D., Massa, M., Luzi, L., Ameri, G., Pacor, F., Puglia, R., & Augliera, P., 2014. Pan-European ground-motion prediction equations for the average horizontal component of PGA, PGV, and 5 to 3.0 s using the RESORCE dataset, *Bulletin of Earthquake Engineering*, **12**(1), 391–430.

Boccaletti, M., Bonini, M., Corti, G., Gasperini, P., Martelli, L., Piccardi, L., Severi, P., & Vannucci, G., 2004. *Seismotectonic map of the Emilia-Romagna Region, Emilia-Romagna Region - SGSS and CNR-IGG*, S.EL.CA Florence.

Boccaletti, M., Corti, G., & Martelli, L., 2010. Recent and active tectonics of the external zone of the Northern Apennines (Italy), *International Journal of Earth Sciences*, **100**, 1331–1348.

Bordoni, P., Azzara, R. M., Cara, F., Cogliano, R., Cultrera, G., Di Giulio, G., Fodarella, A., Milana, G., Pucillo, S., Riccio, G., Rovelli, A., Augliera, P., Luzi, L., Lovati, S., Massa, M., Pacor, F., Puglia, R., & Ameri, G., 2012. Preliminary results from EMERSITO, a rapid response network for site-effect studies, *Annali di Geofisica*, **55**(4).

Burrato, P., Vannoli, P., Fracassi, U., Basili, R., & Valensise, G., 2012. Is blind faulting truly invisible? Tectonic-controlled drainage evolution in the epicentral area of the May 2012, Emilia-Romagna earthquake sequence (Northern Italy), *Annals of Geophysics*, **55**(4).

Castro, R. R., Pacor, F., Puglia, R., Ameri, G., Letort, J., Massa, M., & Luzi, L., 2013. The 2012 May 20 and 29, Emilia earthquakes (Northern Italy) and the main aftershocks: S-wave attenuation, acceleration source functions and site effects, *Geophysical Journal International*, **195**(1), 597–611.

CEN, 2004. Eurocode 8: Design provisions for earthquake resistance of structures, part 1.1: General rules, seismic actions and rules for buildings.

Chaljub, E., Komatitsch, D., Vilotte, J. P., Capdeville, Y., Valette, B., & Festa, G., 2007. Spectral element analysis in seismology, in *Advances in wave propagation in heterogeneous media*, vol. 48 of **Advances in Geophysics**, pp. 365–419, eds Wu, R.-S. & Maupin, V., Elsevier - Academic Press, London, UK.

De Basabe, J. D., Sen, M. K., & Wheeler, M. F., 2008. The interior penalty discontinuous Galerkin method for elastic wave propagation: grid dispersion, *Geophys. J. Int.*, **175**(1), 83–93.

DPC-INGV Project S2, 2012. Constraining observations into seismic hazard.

Faccioli, E., Maggio, F., Paolucci, R., & Quarteroni, A., 1997. 2D and 3D elastic wave propagation by a pseudo-spectral domain decomposition method, *Journal of Seismology*, **1**(3), 237–251.

Fantoni, R. & Franciosi, R., 2010. Tectono-sedimentary setting of the Po Plain and Adriatic foreland, *Rend. Fis. Acc. Lincei*, **21**, S197S209.

Galli, P., Castenetto, S., & Peronace, E., 2012. Rilievo Macrosismico MCS speditivo, Terremoti dell'Emilia - Maggio 2012, Tech. rep., Dipartimento della Protezione Civile, Final Report.

Göddeke, D., Komatitsch, D., & Möller, M., 2014. Finite and spectral element methods on unstructured grids for flow and wave propagation methods, in *Numerical Computations with GPUs*, chap. 9, pp. 183–206, ed. Kindratenko, V., Springer.

Govoni, A., Marchetti, A., De Gori, P., Di Bona, M., Lucente, F., Improta, L., Chiarabba, C., Nardi, A., Margheriti, L., Piana Agostinetti, N., Di Giovambattista, R., Latorre, D., Anselmi, M., Ciaccio, M., Moretti, M., Castellano, C., & Piccinini, D., 2014. The 2012 Emilia seismic sequence (Northern Italy): imaging the thrust fault system by accurate aftershock location, *Tectonophysics*, in press.

Herrero, A. & Bernard, P., 1994. A kinematic self-similar rupture process for earthquakes, *Bull. Seismol. Soc. Am.*, **84**(4), 1216–1228.

Hesthaven, J. & Warburton, T., 2008. *Nodal discontinuous Galerkin methods*, vol. 54 of **Texts in Applied Mathematics**, Springer, Berlin.

Hisada, Y. & Bielak, J., 2003. A theoretical method for computing near-fault ground motions in layered half-spaces considering static offset due to surface faulting, with a physical interpretation of fling step and rupture directivity, *Bull. Seismol. Soc. Am.*, **93**(3), 1154–1168.

Käser, M. & Dumbser, M., 2006. An arbitrary high order discontinuous Galerkin method for elastic waves on unstructured meshes I: The two-dimensional isotropic case with external source terms, *Geophysical Journal International*, **166**(2), 855–877.

Komatitsch, D. & Tromp, J., 1999. Introduction to the spectral-element method for 3-D seismic wave propagation, *Geophys. J. Int.*, **139**(3), 806–822.

Komatitsch, D., Tsuboi, S., & Tromp, J., 2005. The spectral-element method in seismology, in *Seismic Earth: Array Analysis of Broadband Seismograms*, vol. 157 of **Geophysical Monograph**, pp. 205–228, eds Levander, A. & Nolet, G., American Geophysical Union, Washington DC, USA.

Luzi, L., Pacor, F., Ameri, G., Puglia, R., Burrato, P., Massa, M., Augliera, P., Franceschina, G., Lovati, S., & Castro, R., 2013. Overview on the strong-motion data recorded during the May–June 2012 Emilia seismic sequence, *Seism. Res. Lett.*, **84**(4), 629–644.

Maday, Y., Mavriplis, C., & Patera, A. T., 1989. Nonconforming mortar element methods: application to spectral discretizations, in *Domain decomposition methods (Los Angeles, CA, 1988)*, pp. 392–418, SIAM, Philadelphia, PA.

Maini, C., 2015. *Near-source seismic displacement evaluation: from data processing to code provisions*, Master Thesis in Geotechnical Engineering, Politecnico di Milano.

Martelli, L. & Molinari, F., 2008. Studio geologico finalizzato alla ricerca di potenziali serbatoi geotermici nel sottosuolo del comune di mirandola, Tech. rep., Regione Emilia-Romagna, Servizio geologico sismico e dei suolo, in italian.

Mazzieri, I., Stupazzini, M., Guidotti, R., & Smerzini, C., 2013. SPEED: SPectral Elements in Elastodynamics with Discontinuous Galerkin: a non-conforming approach for 3D multi-scale problems, *Int. J. Numer. Meth. Eng.*, **95**(12), 991–1010.

Milana, G., Bordoni, P., Cara, F., Di Giulio, G., Hailemikael, S., & Rovelli, A., 2014. 1D velocity structure of the Po River plain (Northern Italy) assessed by combining strong motion and ambient noise data, *Bull. Earth. Eng.*, **12**, 2195–2209.

Moczo, P., Kristek, J., & Galis, M., 2014. *The Finite-Difference Modelling of Earthquake Motions: Waves and Ruptures*, Cambridge University Press.

Molinari, I., Argnani, A., Morelli, A., & Basini, P., 2015. Development and testing of a 3D seismic velocity model of the Po Plain sedimentary basin, Italy, *Bull. Seismol. Soc. Am.*, **105**(2A), 753–764.

Munich RE, 2015. NatCatService, http://www.munichre.com/natcatservice.

Paolucci, R., Mazzieri, I., Smerzini, C., & Stupazzini, M., 2014. Physics-based earthquake ground shaking scenarios in large urban areas, in *Perspectives on European Earthquake Engineering and Seismology, Geotechnical, Geological and Earthquake Engineering*, vol. 34, chap. 10, ed. Ansal, A., Springer.

Patera, A. T., 1984. A spectral element method for fluid dynamics: laminar flow in a channel expansion, *J. Comput. Phys.*, **54**(3), 468 – 488.

Peyrusse, F., Glinsky, N., Gélis, C., & Lanteri, S., 2014. A nodal discontinuous galerkin method for site effects assessment in viscoelastic media-verification and validation in the nice basin, *Geophysical Journal International*, **199**(1), 315–334.

Pezzo, G., Merryman Boncori, J. P., Tolomei, C., Salvi, S., Atzori, S., Antonioli, A., Trasatti, E., Novali, F., Serpelloni, E., Candela, L., & Giuliani, R., 2013. Coseismic deformation and source modeling of the May 2012 Emilia (Northern Italy) earthquakes, *Seism. Res. Lett.*, **84**(4), 645–655.

Pieri, M. & Groppi, G., 1981. Subsurface geological structure of the Po Plain, Italy, *CNR, Progetto Finalizzato Geodinamica*, **414**, 1–13.

Quarteroni, A., Sacco, R., & Saleri, F., 2007. *Numerical mathematics*, vol. 37 of **Texts in Applied Mathematics**, Springer-Verlag, Berlin, 2nd edn.

RER, 1998. *Riserve idriche sotterranee della Regione Emilia-Romagna*, Regione Emilia Romagna, Servizio Geologico Sismico e dei Suoli & ENI-AGIP, Di Dio (Ed.), S.EL.CA., Florence, 120 pages.

Salvi, S., Tolomei, C., Boncori, J. M., Pezzo, G., Atzori, S., Antonioli, A., Trasatti, E., Giuliani, R., Zoffoli, S., & Coletta, A., 2012. Activation of the SIGRIS monitoring system for ground deformation mapping during the Emilia 2012 seismic sequence, using COSMO-SkyMed InSAR data, *Annals of Geophysics*, **55**(4).

Seriani, G., Priolo, E., & Pregarz, A., 1995. Modelling waves in anisotropic media by a spectral element method, *Proceedings of the third international conference on mathematical and numerical aspects of wave propagation*, pp. 289–298.

Stacey, R., 1988. Improved transparent boundary formulations for the elastic-wave equation, *Bull. Seismol. Soc. Am.*, **78**(6), 2089–2097.

Stupazzini, M., Paolucci, R., & Igel, H., 2009. Near-fault earthquake ground-motion simulation in the Grenoble valley by a high-performance spectral element code, *Bulletin of the Seismological Society of America*, **99**(1), 286–301.

Tizzani, P., Castaldo, R., Solaro, G., Pepe, S., Bonano, M., Casu, F., Manunta, M., Manzo, M., Pepe, A., Samsonov, S., Lanari, R., & Sansosti, E., 2013. New insights into the 2012 Emilia (Italy) seismic sequence through advanced numerical modeling of ground deformation InSAR measurements, *Geophys. Res. Lett.*, **40**(10), 1971–1977.

Villani, M., Faccioli, E., Ordaz, M., & Stupazzini, M., 2014. High-resolution seismic hazard analysis in a complex geological configuration: the case of the Sulmona basin in Central Italy, *Earthquake Spectra*, **30**(4), 1801–1824.

Wilcox, L. C., Stadler, G., Burstedde, C., & Ghattas, O., 2010. A high-order discontinuous Galerkin method for wave propagation through coupled elastic-acoustic media, *J. Comput. Phys.*, **229**(24), 9373 – 9396.

MOX Technical Reports, last issues

Dipartimento di Matematica
Politecnico di Milano, Via Bonardi 9 - 20133 Milano (Italy)

22/2015 Bonaventura, L.; Ferretti, R.
Flux form Semi-Lagrangian methods for parabolic problems

21/2015 Arena, M.; Azzone, G.; Secchi, P.; Vantini, S.
Reputational risk and corporate finance: A multi-event model

20/2015 Antonietti, P.F.; Formaggia, L.; Scotti, A.; Verani, M.; Verzotti, N.
Mimetic finite difference approximation of flows in fractured porous media

19/2015 Palamara, S.; Lange, M.; Vergara, C.; Lassila, T.; Frangi, A.F.; Quarteroni, A.
A coupled 3D-1D numerical monodomain solver for cardiac electrical activation in the myocardium with detailed Purkinje network

17/2015 Nestola, M.G.C.; Faggiano, E.; Vergara, C.; Lancellotti, R.M.; Ippolito, S,; Filippi, S.; Quartero
Computational comparison of aortic root stresses in presence of stentless and stented aortic valve bio-prostheses

18/2015 Masci, C,; Ieva, F.; Agasisti, T.; Paganoni, A.M.
Bivariate multilevel models for the analysis of mathematics and reading pupils' achievements

16/2015 Fumagalli, I.; Manzoni, A.; Parolini, N.; Verani, M.
Reduced basis approximation and a posteriori error estimates for parametrized elliptic eigenvalue problems

15/2015 Taffetani, M.; de Falco, C.; Penta, R.; Ambrosi, D.; Ciarletta, P.
Biomechanical modelling in nanomedicine: multiscale approaches and future challenges

14/2015 Canuto, C.; Nochetto, R.H.; Stevenson R,; Verani, M.
Convergence and Optimality of hp-AFEM

13/2015 Bartezzaghi, A.; Dedè, L.; Quarteroni, A.;
Isogeometric Analysis of High Order Partial Differential Equations on Surfaces